Limiting Temperatures of Spherical Shock Wave Implosion

Michael Liverts* and Nicholas Apazidis
Department of Mechanics, KTH Royal Institute of Technology, 100 44 Stockholm, Sweden
(Received 25 August 2015; published 5 January 2016)

Spherical shock wave implosion in argon is studied both theoretically and experimentally. It is shown that as the strength of the converging shock increases the nonideal gas effects become dominant and govern the evolution of thermal and transport gas properties limiting the shock acceleration, lowering the gas adiabatic index and the achievable energy density at the focus. Accounting for multiple-level ionization, excitation, Coulomb interaction and radiation effects, the limiting equilibrium temperatures to be achieved during the shock implosion are estimated. Focal temperatures of the order of 30 000 K are measured in experiments where converging spherical shock waves are created using a conventional gas-dynamic shock tube facility.

DOI: 10.1103/PhysRevLett.116.014501

Converging shock waves (CSWs) can be found in a broad range of situations, from astronomical size events like supernova collapse [1], to microscopic events such as gas bubble sonoluminescence [2]. A continuing interest in CSW studies is also motivated by applications demanding high energy concentration, e.g., inertial confinement fusion [3,4]. The well-known self-similarity solution [5,6] for cylindrical and spherical convergence describes a continuously accelerating CSW with ever increasing temperature and pressure as it approaches the focal singularity. Indeed, assuming the perfect gas law and the ideally shaped cylindrical and/or spherical shock wave steep front, an infinite energy concentration is expected at the implosion focus. In reality, however, once the shock acquires some critical intensity, the gas behind the shock front can no longer be described as perfect. Depending on the gas type and local thermodynamic conditions, the corresponding real gas mechanisms are initiated [7] and result in a substantially reduced shock wave intensity. The establishment of thermodynamic equilibrium requires a certain relaxation time increasing the shock front thickness (see, e.g., Refs. [8–10] considering planar shocks). This prevents the CSW from collapsing into a singular point and thus results in a less effective energy concentration.

Compared to cylindrical [11–16], spherical convergence is a more powerful method of shock amplification. In terms of experimental realization it also presents a harder challenge. Spherical CSWs can be generated by reflecting a blast wave off a spherical surface, thus reversing it back to focus at the chamber center. Using this technique, experiments have been conducted to measure the temperature at the implosion focus and the highest reported were in the range 15 000–17 000 K [17–20]. Recently, in search of ultrahigh pressure generation, CSWs were produced in water by an electrically induced explosion of wire arrays. The pressures of 400 GPa and 2 TPa were estimated at the focus of cylindrical and spherical CSWs correspondingly [21,22].

Despite the extensive data obtained during a few decades on the nonideal gas effects in planar strong shocks [7–9,23–25], the application of this field towards CSWs seems lacking. In this Letter, we aimed to explore the range of maximum possible temperatures that can be expected during the spherical CSW implosion in gas. We demonstrate, both theoretically and experimentally, that as the strength of the CSW increases the nonideal gas effects become dominant and govern the evolution of gas properties. The discussion is limited by considering a monatomic gas, argon, therefore accounting for ionization, excitation, radiation, and Coulomb interaction effects. The proposed technique can be safely applied to other gases, accounting for corresponding real gas mechanisms.

The experiments were conducted in a circular shock tube with helium and argon as the driver and test gas, respectively. The shock tube channel was followed by a converging test section (see Figs. 1) composed of the transformation segment (TS) and the conical segment (CS). The TS was designed to smoothly transform initially planar shock into a CSW of a spherical shape, avoiding Mach reflections and subsequent breakup of the front symmetry (see Refs. [26,27] for cylindrical and spherical shapes, respectively). The following CS with an inner

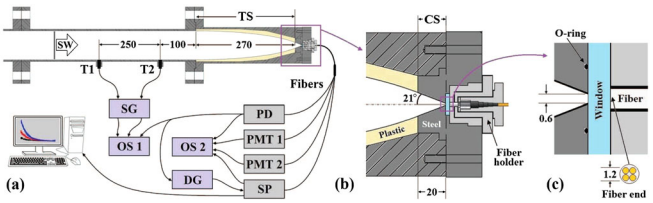

FIG. 1. (a) Schematic diagram of shock tube and diagnostic setup. SG signal conditioner, OS oscilloscope, DG delay generator, PD photodiode, PMTs photomultiplier tubes equipped with bandpass interference filters (220 and 405 nm CWL), SP spectrometer. (b) Zoomed area of conical segment. (c) Zoomed conical tip with optical window and fiber details.

axisymmetric conical profile [Fig. 1(b)] ended in a circular opening [Fig. 1(c)] sealed with a sapphire window. The major advantages of this technique over the blast reflection methods are the abilities to (1) create the optimal spherical CSW front, and (2) directly access for measurements the implosion core where the gas is initially undisturbed.

The incident planar shock wave, Mach number M_0, was registered by pressure transducers $T1$ and $T2$. As the shock converges towards the CS tip, the conditions become extreme so that the gas intensively glows. The light flash collected through the window by optical fibers was separately transferred into a diagnostic setup as shown in Fig. 1(a) (for more details on the experimental setup see Ref. [27]).

For shock propagation in the TS, a numerical simulation of Euler equations considering perfect gas was used [27]. The initial spherical shock Mach number M_S, plotted vs M_0 in Fig. 2(a), was determined from the shock front pressure amplitude calculated at the instant of CSW entering the CS [see inset image in Fig. 2(a)]. The calculations showed that the TS shape fulfilled the design criteria well, whereas an almost spherical shock front entered the CS. If Δr_0 is the deviation from the initial CSW mean radius $r_0 = 22$ mm, the maximum deviation $\Delta r_0/r_0$ did not exceed 0.005 in computations. To verify these estimations in experiments, the CS was replaced by a segment with additional pressure transducer $T3$ directed towards the incident flow [see inset image in Fig. 2(b)]. $T3$ was mounted inside an end wall with a spherically shaped face area to ensure normal reflection of the shock wave. The calculation domain was constructed similarly. Figure 2(b) demonstrates the pressure traces registered both numerically and experimentally. The times of shock arrivals, the pressure amplitudes, and the dynamics of the reflection process were well predicted for various initial shock intensities, implicitly verifying the efficient plane-to-spherical shock transformation and M_S estimations.

In the CS, ideal calculations cannot predict the extreme conditions as the shock wave reaches and reflects at the window. Because of the geometry from here on, the problem can be considered as one-dimensional with initial conditions obtained from the numerical simulation. Geometric shock dynamics approximation was adopted with modified shock jump relations accounting for nonideal gas effects [28]. The essential assumption behind Whitham's approach [29] (also known as the CCW approximation after Chester-Chisnell-Whitham) is based on the assumption that in the case of an accelerating CSW the interaction with the flow behind it can be ignored. Therefore, the CSW motion can be approximated by integrating the equation governing the flow along the C_+ characteristic. The ratio of the shock wave radii, r, at two consecutive time instants, t_1 and t_2 can be expressed as

$$\frac{r_2}{r_1} = \exp\left[-\frac{1}{2}\left(\int_1^2 \frac{u+a}{\rho a^2 u}dp + \int_1^2 \frac{u+a}{au}du\right)\right], \quad (1)$$

where ρ,u, and p are the gas density, velocity, and pressure, respectively, and a is the speed of sound.

The variables necessary for solving Eq. (1) were obtained from equations of mass, momentum, and energy conservation across the shock front. In a thermodynamic equilibrium (TE) the gas composed of electrons, ions, atoms, and photons can be described by statistical mechanics, where equilibrium distributions are characterized by the same temperature. When photons escape from an ionized gas the balances involving electrons, ions, and atoms are inevitably affected. However, if the energy loss by radiation is small, the Saha-Boltzmann and Maxwell distributions are still a valid description of the system and a local thermal equilibrium (LTE) is settled. Assuming LTE, the distribution of atoms and ionization products was calculated using the Saha equations:

$$\frac{\alpha_{i+1}\alpha_e}{\alpha_i} = \left(\frac{2\pi m_e kT}{h^2}\right)^{3/2}\frac{m_A}{\rho}\frac{2Q_{i+1}}{Q_i}\exp\left(-\frac{I_{i+1}^{\mathrm{eff}}}{kT}\right), \quad (2)$$

where m_e is the electron's mass, k is Boltzmann's constant, h is Planck's constant, m_A is the mass of the argon atom, α_e is the electron concentration per number of atoms, α_i is the ion concentration in ionization stage i, Q_i is the electronic partition function in ionization stage i, and T is the absolute equilibrium temperature. The ith effective ionization potential is reduced due to Coulomb interactions $I_i^{\mathrm{eff}} = I_i - \Delta I_i$,

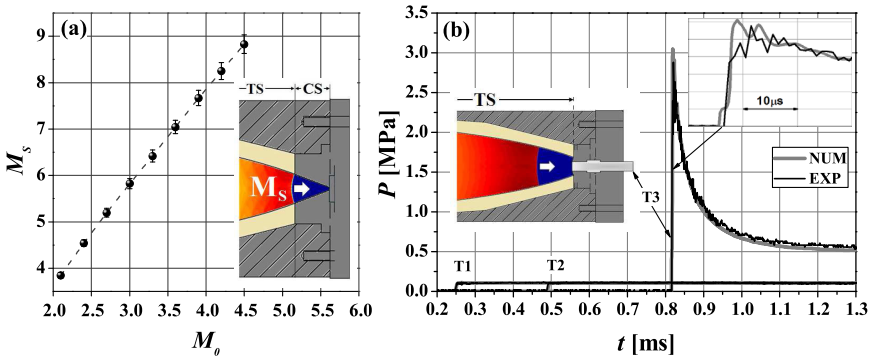

FIG. 2. (a) M_S vs M_0. (b) Experimental and numerical pressure traces at $T1$–$T3$, $M_0 = 3.25$, $p_0 = 10$ kPa.

where $\Delta I_i = (i+1)e^2/4\pi\varepsilon_0 r_D$, e is the electron charge, ε_0 is the vacuum permittivity, and r_D is the Debye screening radius [30].

The specific internal energy per unit mass of a monatomic gas accounting for nonideal gas effects can be written as

$$e = \frac{3}{2}(1+\alpha_e)RT + \frac{1}{m_A}\left[\sum_{i=1}^{l}\alpha_i\sum_{j=1}^{i} I_j^{\mathrm{eff}} + \sum_{i=0}^{l}\alpha_i\frac{U_i}{Q_i}\right] + \frac{\sigma}{\rho}T^4 - \frac{kT}{8\pi\rho r_D^3}, \quad (3)$$

where R is the specific gas constant, $\sigma = 7.57\times 10^{-16}\ \mathrm{J\,m^{-3}\,K^{-4}}$, and U_i is the total excitation energy of an atom or ion in ionization stage i. The terms represent, respectively, translation, ionization, excitation, radiation, and the last term is due to Coulomb interactions. In computations of Q_i and U_i the summation is performed over all the available spectroscopic data [31] including all levels for which $e_i^j < I_i^{\mathrm{eff}}$, where e_i^j is the excitation energy of level j in ionization stage i. In general, the upper bound for l is the gas atomic number, while for the temperatures considered herein it was limited to $l = 3$.

The equation of state including Coulomb correction and radiation pressure is

$$p = (1+\alpha_e)\rho RT - \frac{kT}{24\pi r_D^3} + \frac{\sigma}{3}T^4. \quad (4)$$

The gas enthalpy is then given by $h = e + p/\rho$. Complimented with charge conservation equations, the resulting nonlinear system was solved using the Newton method iterative approach. The equilibrium speed of sound and heat capacities behind the CSW were evaluated numerically according to $a^2 = c_p/c_v(\partial p/\partial\rho)_T$, where $c_p = (\partial h/\partial T)_p$, and $c_v = (\partial e/\partial T)_v$. The CSW was propagated along the CS governed by Eq. (1), and as a last step the reflected shock jump relations were applied to estimate the maximum values of the temperature behind the reflected shock.

Two shock front trajectories referring to perfect and nonideal gas conditions are plotted in Fig. 3. Self-similar curves are added for comparison according to Guderley's [5] solution $r = r_0(1 - t/t_0)^{\chi}$, where r is the radius and t is the time; r_0 and t_0 are the initial radius and time of focusing, respectively. The self-similarity constant for spherical shocks in argon ($\gamma = 5/3$) is $\chi = 0.688$, which agrees well with the CCW approximation in perfect gas (for further discussions of the CCW approximation see, e.g., Ref. [32–34]). The shock trajectory in the non-ideal gas was successfully fitted with $\chi = 0.752$, which corresponds to a self-similar solution of a spherical shock converging in ideal gas with $\gamma = 1.2$ [33]. Based on the herein thermal data, the adiabatic index was computed and approached

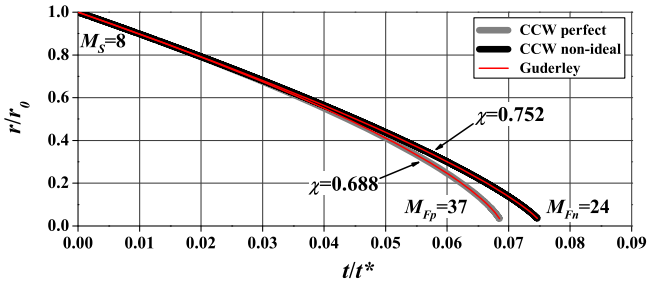

FIG. 3. Calculated trajectories of the initially identical ($M_S = 8$) converging spherical shock waves in perfect and nonideal gases; $t^* = r_0/a_0$.

$\gamma \approx 1.325$ once the gas was noticeably ionized. Although the obtained χ is overestimated, it satisfies the correct trend and presumably is the average effective value describing the shock front trajectory in the real gas conditions. The acceleration of CSW in nonideal gas is also weaker. The calculation shows that two identical shocks starting with initially equal Mach number $M_S = 8$ from the same initial radius $r_0 = 22$ mm, acquire substantially different focal Mach numbers M_F as they approach the final radius $r_F = 0.78$ mm (just before the reflection off the window). It should be noted that to make the quasiequilibrium assumption valid this study deals with sufficiently strong shocks at the focal region ensuring fast equilibration rates, e.g., for $M_F = 24$ the relaxation time is ~30 ns [10], which is shorter than the time scale of compression $[u\,d(\ln A)/dr]^{-1} \approx 100$ ns.

Figure 4(a) demonstrates concentrations of the gas species behind the CSW as functions of the shock radius (bottom axis) and the varying Mach number, M (top axis). The results show that the gas composition begins to deviate from the perfect case at Mach numbers $M > 10$ and/or shock radii $r < 10$ mm, where the number of singly ionized atoms becomes noticeable. During the incident shock convergence up to the location of the CS tip window only the first ionization occurs; however, after reflection the conditions are extreme enough to trigger the second ionization also. The energy fractions of each of the considered effects are shown in Fig. 4(b). It is evident that the dominant mechanism is the gas ionization, which acquires fractions of order of 70% of the total gas energy. The least contributing mechanism is the radiation, which is negligible in the considered range of CSW intensities.

The electron density variation can be roughly described by $\dot{n}_e = N_{\mathrm{ion}} - N_{\mathrm{rec}}$, where N_{ion} and N_{rec} are the ionization and recombination rates, respectively. When $\dot{n}_e > 0$ the ionization process prevails, thus the gas is ionizing; on the contrary, when $\dot{n}_e < 0$ the gas is recombining. When $\dot{n}_e = 0$, the ionization and recombination processes are balanced, and the conditions can be assumed to satisfy TE. To trace the details of the approach to TE a spectrum region 220 ± 5 nm was chosen. Since this region does not contain any strong argon lines the data in Fig. 5(a) may be

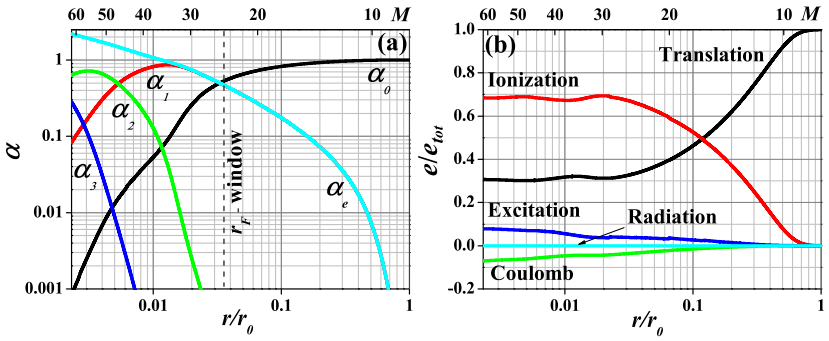

FIG. 4. (a) Concentrations of neutral atoms, ions, and electrons per total number of atoms; and (b) specific energy fractions of the total gas energy e/e_{tot}, during the spherical shock convergence.

also referred to as the time variation of the squared electron density [7]. The obtained signals rise from zero and flatten off to equilibrium values, which maintain for a short period of 100–200 ns and thereafter fall monotonically. A closer look at Fig. 5(a) reveals that it takes about 250–400 ns for the light signal to rise from essentially zero to a maximum value, which is well above the instrumentation possible response times (~10 ns). Since the gas enthalpy during the reflection is almost doubled, the gas should ionize and become luminous more rapidly than the gas behind the incident shock, so the rise time is mainly governed by the incident CSW relaxation zone. The light history shown in Fig. 5(a) can be divided into three stages of ionizing, equilibrium and recombining gas (marked τ_{ion}, τ_{TE}, and τ_{rec}, correspondingly). The times τ_{ion} were examined throughout several experimental data and showed to decrease with increasing shock intensity. During the period of the short plateau level, i.e., τ_{TE}, a spectrum of the light flash was measured with a 100 ns exposure gate. Assuming equilibrium during this period, the gas temperature at the tip of the CS was deduced from the Planck's fit to the radiation spectrum: $I_\lambda(A,\lambda,T) = A\lambda^{-5}[\exp(hc/\lambda kT) - 1]^{-1}$, where I_λ is the intensity per unit wavelength λ, h is the Planck's constant, c is the speed of light, and A is the fitting parameter.

Figure 5(b) demonstrates three experimental spectra obtained in tests with different initial Mach numbers, namely, $M_S = 5.21$, 6.25, and 7.57. Least square fits to the spectra show good agreement with Planck's law and the resulting temperatures are 18 200, 23 400 and 31 000 K, accordingly. Figure 5(a) demonstrates the corresponding spectrometer exposure gates on each curve, verifying that the temperature was measured during the assumed equilibrium in each run. To ensure that the temperature value was maximum the instant of the measurement was also matched with the peak value of the ratio of two signals acquired from PMTs (two distinct wavelengths 220 and 405 nm).

To summarize, Fig. 6 presents the data consisting of various maximum equilibrium temperatures acquired in tests with three different initial test gas pressures, $p_0 = 5$, 10, and 20 kPa. The top curve (note the axis breaks) refers to the calculation treating argon as a perfect gas. It is evident that in the ideal conditions, the data are significantly overestimated and enormous temperatures are predicted in the range 100 000–400 000 K. Including the nonideal gas effects, the predicted temperatures are substantially reduced and are in close proximity to the points obtained experimentally. It is evident from Fig. 6 that the trend of the observed temperatures agrees with calculations, namely, for a fixed Mach number M_S, the higher the initial pressure and density of argon, the higher the maximum temperature behind the reflected shock, the reason for which is the weaker ionization degree in denser gases.

The experimental data are in close agreement with the modified CCW calculations; however, small discrepancies are present. Indeed, the used approximation including the nonideal gas effects treats the problem as an idealized scenario of a spherical shock wave implosion. The problem is considered as one dimensional with a shock front of zero thickness having a perfect spherical symmetry. In reality, the shock front including the relaxation zone is thick, it reflects from the window gradually and escapes away

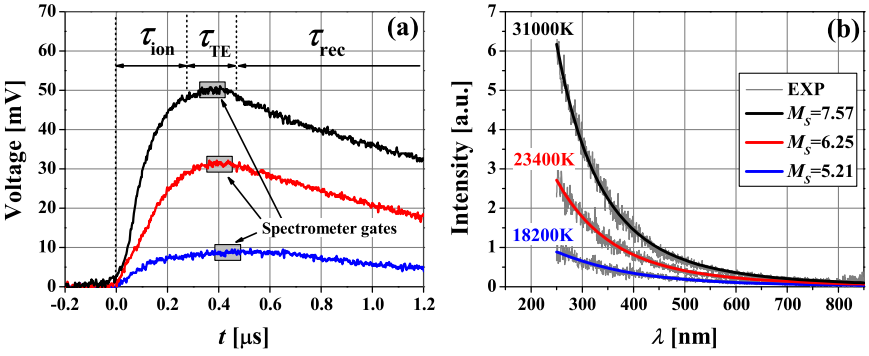

FIG. 5. (a) 220 nm wavelength intensity. (b) Flash light spectra fitted with Planck's law.

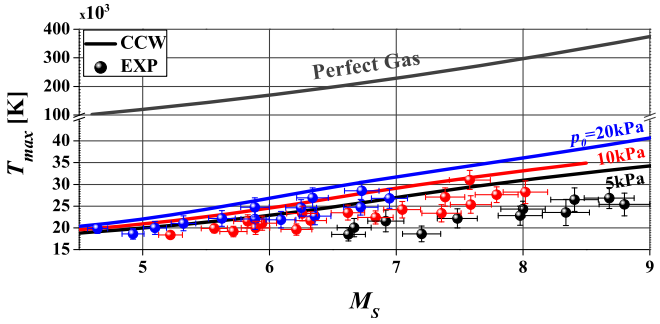

FIG. 6. Temperature at the CS focus vs incident spherical shock Mach number M_S.

leaving the cooler gas behind it during the spectra measurement. The relaxation length grows with decreasing gas pressure and density, hence providing larger discrepancies for lower downstream pressures. Shock instability, inevitable boundary layer effects, thermal effects at the window, etc., are also possible: however, Fig. 6 promises that the corrections would be minor.

The results clearly show that the dominant mechanism responsible for the correct description of the CSW implosion is the gas (argon) ionization. The presented calculation approach serves efficiently for predicting the limiting shock intensities. Indeed the gas (heavy particles) nonequilibrium temperature immediately behind the reflected shock front should rise to values well above the measured temperatures. However, those rapidly relax during a rather short period, which would be even shorter for stronger shocks. It was shown that in the case of argon, its thermal and transport properties begin to deviate significantly from the perfect gas law at shock Mach numbers $M > 10$. The stronger the shock the more pronounced the deviation; e.g., extending the calculation towards the shock radius $r = 50\ \mu$m the perfect gas approach predicts temperatures of order of 1.5×10^6 K behind the incident shock front with Mach number $M \approx 125$, while in the nonideal case it is limited to 55 000 K and $M \approx 62$. This suggests that the ionization is an inherent and dominant feature defining an upper bound for achievable temperature levels of a converging shock wave at the focal region.

This work was supported by Vetenskapsrådet. We thank Dr. N. Tillmark for fruitful discussions.

*liverts@mech.kth.se

[1] S. Woosley and T. Janka, Nat. Phys. **1**, 147 (2005).
[2] D. Flannigan and K. Suslick, Nat. Phys. **6**, 598 (2010).
[3] R. Betti, C. D. Zhou, K. S. Anderson, J. L. Perkins, W. Theobald, and A. A. Solodov, Phys. Rev. Lett. **98**, 155001 (2007).
[4] C. J. Davie and R. G. Evans, Phys. Rev. Lett. **110**, 185002 (2013).
[5] G. Guderley, Luftfahrtforschung **19**, 302 (1942).
[6] L. D. Landau and E. M. Lifshitz, *Fluid Mechanics, Course of Theoretical Physics*, edited by J. B. Sykes and W. H. Reid (Pergamon Press, Oxford, New York, 1987), p. 406.
[7] Ya. B. Zel'dovich and Yu. P. Raizer, *Physics of Shock Waves and High-Temperature Hydrodynamic Phenomena*, edited by W. D. Hayes and R. F. Probstein (Dover, Mineola, New York, 2002), pp. 176,505.
[8] H. Petschek and S. Byron, Ann. Phys. (N.Y.) **1**, 270 (1957).
[9] J. W. Bond, Phys. Rev. **105**, 1683 (1957).
[10] L. Biberman, A. Mnatsakanyan, and I. Yakubov, Sov. Phys. Usp. **13**, 728 (1971).
[11] R. W. Perry and A. Kantrowitz, J. Appl. Phys. **22**, 878 (1951).
[12] K. Takayama, H. Kleine, and H. Grnig, Exp. Fluids **5**, 315 (1987).
[13] V. Eliasson, N. Apazidis, and N. Tillmark, Shock Waves **17**, 29 (2007).
[14] V. Eliasson, N. Tillmark, A. J. Szeri, and N. Apazidis, Phys. Fluids **19**, 106106 (2007).
[15] M. Kjellander, N. Tillmark, and N. Apazidis, Phys. Fluids **22**, 046102 (2010).
[16] M. Kjellander, N. Tillmark, and N. Apazidis, Phys. Fluids **23**, 116103 (2011).
[17] D. E. Roberts and I. I. Glass, Phys. Fluids **14**, 1662 (1971).
[18] R. A. Roig and I. I. Glass, Phys. Fluids **20**, 1651 (1977).
[19] T. Saito and I. I. Glass, Proc. R. Soc. A **384**, 217 (1982).
[20] S. H. R. Hosseini and K. Takayama, J. Fluid Mech. **530**, 223 (2005).
[21] A. Fedotov-Gefen, S. Efimov, L. Gilburd, G. Bazalitski, V. Tz. Gurovich, and Ya. E. Krasik, Phys. Plasmas **18**, 062701 (2011).
[22] O. Antonov, L. Gilburd, S. Efimov, G. Bazalitski, V. Tz. Gurovich, and Ya. E. Krasik, Phys. Plasmas **19**, 102702 (2012).
[23] E. J. Morgan and R. D. Morrison, Phys. Fluids **8**, 1608 (1965).
[24] K. Terao, M. Hozaka, and H. Kaitoh, Jpn. J. Appl. Phys. **22**, 735 (1983).
[25] M. Mond, I. Rutkevich, and E. Toffin, Phys. Rev. E **56**, 5968 (1997).
[26] Z. Zhai, C. Liu, F. Qin, J. Yang, and X. Luo, Phys. Fluids **22**, 041701 (2010).
[27] M. Kjellander, N. Tillmark, and N. Apazidis, Phys. Fluids **24**, 126103 (2012).
[28] M. Kjellander, N. Tillmark, and N. Apazidis, Phys. Fluids **22**, 116102 (2010).
[29] G. B. Whitham, *Linear and Nonlinear Waves* (Wiley, New York, 1974), p. 265.
[30] H. R. Griem, Phys. Rev. **128**, 997 (1962).
[31] A. Kramida, Y. Ralchenko, J. Reader, and NIST-Team, NIST Atomic Spectra Database (version 5.2), [Online] (2014).
[32] H. G. Hornung, D. I. Pullin, and N. Ponchaut, Acta Mech. **201**, 31 (2008).
[33] V. Tz. Gurovich, A. Grinenko, and Ya. E. Krasik, Phys. Rev. Lett. **99**, 124503 (2007).
[34] S. D. Ramsey, J. R. Kamm, and J. H. Bolstad, Int. J. Comput. Fluid Dyn. **26**, 79 (2012).